arXiv:1604.00185v1 [astro-ph.GA] 1 Apr 2016

Broad [CII] line wings as tracer of molecular and multi-phase outflows in infrared bright galaxies

A.W. Janssen[1], N. Christopher[2,3], E. Sturm[1], S. Veilleux[4,5], A. Contursi[1], E. González-Alfonso[6], J. Fischer[7], R. Davies[1], A. Verma[2], J. Graciá-Carpio[1], R. Genzel[1], D. Lutz[1], A. Sternberg[8], L. Tacconi[1], L. Burtscher[1], A. Poglitsch[1]

janssen@mpe.mpg.de

ABSTRACT

We report a tentative correlation between the outflow characteristics derived from OH absorption at 119 μm and [CII] emission at 158 μm in a sample of 22 local and bright ultraluminous infrared galaxies (ULIRGs). For this sample we investigate whether [CII] broad wings are a good tracer of molecular outflows, and how the two tracers are connected. Fourteen objects in our sample have a broad wing component as traced by [CII], and all of these also show OH119 absorption indicative of an outflow (in 1 case an inflow). The other eight cases, where no broad [CII] component was found, are predominantly objects with no OH outflow or a low-velocity ($\leq 100\,\mathrm{km\ s^{-1}}$) OH outflow. The full width at half maximum (FWHM) of the broad [CII] component shows a trend with the OH119 blue-shifted velocity, although with significant scatter. Moreover, and despite large uncertainties, the outflow masses derived from OH and broad [CII] show a 1:1 relation. The main conclusion is therefore that broad [CII] wings can be used to trace molecular outflows. This may be particularly relevant at high redshift, where the usual tracers of molecular gas (like low-J CO lines) become hard to observe. Additionally, observations of blue-shifted Na I D $\lambda\lambda 5890, 5896$ absorption are available for ten of our sources. Outflow velocities of Na I D show a trend with OH velocity and broad [CII] FWHM. These observations suggest that the atomic and molecular gas phases of the outflow are connected.

[1]Max-Planck-Institute for Extraterrestrial Physics (MPE), Giessenbachstraße 1, 85748 Garching, Germany

[2]Oxford University, Dept. of Astrophysics, Oxford OX1 3RH, UK

[3]School of Sciences, European University Cyprus, Diogenes Street, Engomi, 1516 Nicosia, Cyprus

[4]Department of Astronomy, University of Maryland, College Park, MD 20742, USA

[5]Joint Space-Science Institute, University of Maryland, College Park, MD 20742, USA

[6]Universidad de Alcalá de Henares, 28871 Alcalá de Henares, Madrid, Spain

[7]Naval Research Laboratory, Remote Sensing Division, 4555 Overlook Ave SW, Washington, DC 20375, USA

[8]Tel Aviv University, Sackler School of Physics & Astronomy, Ramat Aviv 69978, Israel

Subject headings: ISM: jets and outflows — galaxies: active — galaxies: evolution — galaxies: starburst

1. INTRODUCTION

Feedback via powerful winds is thought to play a critical role in galaxy evolution. Without any form of feedback, galaxy evolution models overpredict star formation in the early universe, and spheroid dominated remnants would predominate in the current universe, which is not observed (Cole 1991). In order to match observations, current models implement, among other things, gas inflows from outside the halo and feedback from stars and active galactic nuclei (AGN). The output is then compared to observables like the galactic stellar mass function, the Tully-Fisher relation, the mass-metallicity relation, and the apparent co-evolution of the central Black Hole (BH) mass with the stellar mass (Murray et al. (2005); Sales et al. (2010); Fabian (2012); Vogelsberger et al. (2013); Heckman & Best (2014), also see Silk (2011) for a short review on this topic). Negative feedback, in the form of winds or outflows, is usually required to match the observations.

In the local universe, outflows have been observed in all types of galaxies and in different gas phases. Ionized gas outflows have been observed in dwarf galaxies (Marlowe et al. 1995; Martin 1998) and Seyfert 2 AGNs (Cecil et al. 1990; Harrison et al. 2014). In ultraluminous infrared galaxies (ULIRGs), outflows are observed in several phases: ionized (Spoon & Holt 2009; Westmoquette et al. 2012; Arribas et al. 2014), molecular (Sakamoto et al. 2009; Fischer et al. 2010; Feruglio et al. 2010; Sturm et al. 2011; Veilleux et al. 2013; Spoon et al. 2013; Cicone et al. 2014) and atomic (Rupke & Veilleux 2013b). Morganti et al. (2005) discuss neutral gas outflows in radio galaxies. Possible drivers of the outflows are stars and/or AGN. Theoretically, star formation has the power to remove significant amounts of gas from a Milky-Way sized galaxy (Efstathiou 2000; Hopkins et al. 2012). Indeed, star formation has been observed to drive outflows in the form of H-alpha bubbles above disk galaxies (Rand 1996). Blue-shifted absorption of Na I D and Mg II in star-forming galaxies may also be driven by star formation (Heckman et al. 2011; Diamond-Stanic et al. 2012), although the star formation rate must reach a certain threshold before any correlations with the outflow properties become apparent (Heckman et al. 2015). In massive galaxies however, star formation alone may not be sufficient to power the outflows which can reach velocities $>> 500\,\mathrm{km\,s^{-1}}$. In ULIRGs outflow velocities can reach $1500\,\mathrm{km\,s^{-1}}$ and AGN are the most probable driver (e.g. Sturm et al. (2011); Cicone et al. (2014); Spoon et al. (2013); Veilleux et al. (2013)).

Detections of such outflows at high redshift would confirm that feedback also played an important role in the early universe. These outflows have been detected at $z > 1$, in type 2 AGN (Alexander et al. 2010; Nesvadba et al. 2011; Harrison et al. 2012; Cano-Díaz et al. 2012), in massive star-forming galaxies (Weiner et al. 2009; Banerji et al. 2011; Genzel et al. 2014; Förster Schreiber et al. 2014) and in radio galaxies (Nesvadba et al. 2008), however mostly in ionized or atomic

gas. Since most mass of a gas-rich galaxy is in molecular form, observations of molecular outflows at high redshift would be most helpful in constraining the role of feedback in the early universe. Candidates for these observations are CO rotational lines and OH rotational lines in absorption, preferably observed with sensitive telescopes like ALMA or NOEMA. However, molecular outflows have not yet been detected in high-J CO lines, and low-J CO lines quickly shift out of the ALMA and NOEMA bands.

The ground state OH $^2\Pi_{3/2}$ 5/2 $\rightarrow$ 3/2 transition at 119 μm, or OH119 for short, probes molecular and to a lesser extent atomic gas (Meijerink & Spaans 2005). OH119 becomes observable with ALMA at z=2 (in the 450 μm atmospheric window in Band 9), but a high S/N and bright continuum is needed to detect the outflow in absorption. ULIRGs are intrinsically bright in the far infrared (FIR), providing the continuum for the OH119 absorption, but not all galaxies have such a bright FIR continuum. Detections of blue-shifted OH119 emission are possible but rare at high redshift (Riechers et al. 2014). Direct observations of molecular outflows at high redshift are therefore challenging.

As an alternative, the collisionally-excited fine structure transition of C^+ $^2P_{3/2}$ $\rightarrow^2$ $P_{1/2}$ at rest frame wavelength of 157.741 μm (hereafter [CII]) may be used. It is one of the brightest lines in spectra of star-forming galaxies, as it is the dominant coolant of the ISM over a wide range of physical conditions. Most [CII] emission is thought to arise in Photodissociation Regions (PDRs) around starforming regions, where the intensity of > 13.6 eV photons has dropped sufficiently for hydrogen to stay atomic, while carbon remains ionized (carbon has a slightly lower ionization potential of 11.26 eV). Pineda et al. (2013) find that in our galaxy about 50% of [CII] emission arises from these PDRs, about 30% arises from CO-dark H_2 gas, about 20% from atomic gas, and only very little from hot ionized gas. [CII] shifts into the 450 μm windows of ALMA at redshifts $z = 1.85$, and in the 0.8 mm band of NOEMA at $z = 4$. High velocity outflows appear as broad wings in the [CII] line profile, and such broad wings have been detected at high redshift, for example in the QSO SDSS J1148+5251 $z = 6.4$ (Maiolino et al. 2012; Cicone et al. 2015).

In this paper, we investigate how well [CII] traces the molecular outflows in ULIRGs, by comparing the outflow velocity and mass retrieved from *Herschel*[1]/PACS observations of [CII] and OH119. The ULIRGs are all gas-rich and most contain an AGN. A short description of the sample is given in Section 2. We then cover the PACS data reduction in Section 3. The [CII] line profiles have been fitted with Gaussian line profiles, and the FHWM of the broad component is compared to the OH blue-shifted velocity in Section 4. In the same Section we compare the FWHM of the broad [CII] component with the AGN luminosity, with the Na I D blue-shifted absorption velocity and with CO(1-0) line profiles. A discussion of the outflow masses and possible connections between the different phases follows in Section 5. We adopt $H_0 = 70\,\mathrm{km\,s^{-1}\,Mpc^{-1}}$ throughout this paper.

[1]Herschel is an ESA space observatory with science instruments provided by European-led Principal Investigator consortia and with important participation from NASA.

2. SAMPLE DESCRIPTION

The sample consists of all 22 local ($z < 0.1$) ULIRGs from the IRAS Revised Bright Galaxy Sample (Sanders et al. 2003); these are objects with $L_{8-1000\,\mu\mathrm{m}} \geq 10^{12}\,L_{\odot}$. IRAS F09111-1007 lies above this luminosity cutoff, but is faint in the PACS range and therefore excluded. We include, however, NGC 6240 and UGC 5101 which are formally slightly below this cutoff, but in any relevant aspect for this study have similar charateristics as the rest of the sample. See Table 1 for the redshifts, coordinates and AGN fractions of the sample. The AGN fractions are estimated using the ratio of the 30 micron to 15 micron flux densities, f_{30}/f_{15} as measured with the Spitzer Infrared Spectrograph, following Veilleux et al. (2009).

Because ULIRGs represent the IR-bright phase of mergers of gas-rich galaxies (Sanders & Mirabel 1996), several objects in our sample have resolved double nuclei related to interaction and merging. All known double nuclei are covered completely by our PACS observations.

3. OBSERVATIONS AND DATA REDUCTION

Observations were made with the Photodetector Array Camera and Spectrometer (PACS) (Poglitsch et al. 2010), on board the Herschel Space Observatory (Pilbratt et al. 2010). Both the OH 119 μm and the [CII] 158 μm spectra have been obtained as part of the *Herschel* guaranteed time key program SHINING (PI: E. Sturm). We reduced and analyzed the OH data in Veilleux et al. (2013), (V13). Because the OH119 line appears either in pure absorption, pure emission, or as a P-Cygni profile, the spectra were fitted with an absorption component, an emission component, or both. (21/22) spectra have absorption features, which are mostly blue-shifted. We will use the velocities of the absorption features of OH in our analysis using the object's v_{50}(abs), v_{84}(abs) and v_{max}(abs) measured by V13 (see Table 2). v_{50}(abs) is the median velocity of the fitted absorption profile, i.e. 50% of the flux arises above (from velocities more positive than) v_{50}(abs), v_{84}(abs) is the velocity above which 84% of the absorption takes place, and v_{max}(abs) is the velocity, above which all absorption takes place. v_{max}(abs) however depends strongly on the fit to the continuum and the signal to noise ratio, and this introduces typical uncertainties of $\pm 200\,\mathrm{km\,s^{-1}}$. We characterise the molecular outflows by their blue-shifted absorption of a FIR continuum. Therefore, only gas along our line of sight to the ULIRG center is traced. The P-Cygni profiles in OH119 and the large number of objects with blue-shifted OH absorption led Sturm et al. (2011) and Veilleux et al. (2013) to the conclusion that the outflows are isotropic, or have at least a large opening angle. Because [CII] appears in emission, such an isotropic outflow would become visible as blue-shifted and red-shifted wings in the line profile.

The [CII] observations were made in PACS range scan mode with a $2600\,\mathrm{km\,s^{-1}}$ velocity range. Because of the instanteneous coverage of $\sim 1650\,\mathrm{km\,s^{-1}}$, the total spectral range is from -2950 to $+2950\,\mathrm{km\,s^{-1}}$, with decreasing S/N towards the edges. The data reduction was done using the standard PACS reduction and calibration pipeline included in HIPE 13, with upsample

Table 1. Sample

Name	Alternative name	z	RA	DEC	$\alpha_{\rm AGN}$ (%)	$\log(L_{AGN})$
IRAS F05189-2524		0.0426	05:21:01.4	−25:21:46	72	12.07
IRAS 07251-0248		0.0876	07:27:37.5	−02:54:55	30	11.92
IRAS F08572+3915		0.0584	09:00:25.0	39:03:56	70	12.05
IRAS 09022-3615		0.0596	09:04:12.8	−36:27:02	55	12.09
UGC 5101	IRAS F09320+6134	0.0394	09:35:48.8	61:21:22	56	11.8
IRAS F10565+2448		0.0431	10:59:17.4	24:32:38	47	11.77
IRAS F12112+0305		0.0733	12:13:47.4	02:48:34	18	11.63
Mrk 231	IRAS F12540+5708	0.0422	12:56:15.0	56:52:17	81	12.51
IRAS 13120-5453		0.0308	13:15:06.2	−55:09:24	33	11.83
Mrk 273	IRAS F13428+5608	0.0378	13:44:41.8	55:53:14	34	11.74
IRAS F14348-1447		0.0830	14:37:37.3	−15:00:20	17	11.64
IRAS F14378-3651		0.0676	14:40:57.8	−37:04:25	21	11.5
IRAS F15250+3608		0.0552	15:26:59.9	35:58:34	42	11.73
Arp 220	IRAS F15327+2340	0.0181	15:34:57.1	23:30:10	5.8	10.98
NGC 6240	IRAS F16504+0228	0.0245	16:52:58.6	02:24:03	56	11.65
IRAS F17207-0014	IRAS 17208-0014	0.0428	17:23:21.4	−00:17:00	≤ 5	≤ 11.15
IRAS F19297-0406		0.0857	19:32:22.1	−04:00:02	23	11.81
IRAS 19542+1110		0.0624	19:56:35.4	11:19:03	26	11.52
IRAS F20551-4250		0.0430	20:58:27.4	−42:38:57	57	11.87
IRAS F22491-1808		0.0778	22:51:49.0	−17:52:27	14	12.05
IRAS F23128-5919	ESO 148-IG 002	0.0446	23:15:46.6	−59:03:14	63	11.89
IRAS F23365+3604		0.0645	23:39:01.7	36:21:14	45	11.87

Note. — Redshifts, coordinates and AGN fractions and luminosities of the observed sample. AGN fractions are calculated from f_{30}/f_{15}, as described in Veilleux et al. (2009).

Table 2. OH and Na I D observations

Name	OH v_{50} $\mathrm{km\,s^{-1}}$	OH v_{84} $\mathrm{km\,s^{-1}}$	OH v_{max} $\mathrm{km\,s^{-1}}$	Na I D range $\mathrm{km\,s^{-1}}$	OH mass $10^8 M_\odot$
IRAS F05189-2524	-327	-574	-850	-402 to -92 (2)	1.27
IRAS 07251-0248	-63	-255	-550	...	...
IRAS F08572+3915	-489	-832	-1100	−700 to -1000 (3)	0.49
IRAS 09022-3615	-153	-297	-650	...	...
UGC 5101	-9	-225	-1200	-16 to 11 (1)	...
IRAS F10565+2448	-267	-489	-950	-309 to -141 (1)	2.99
IRAS F12112+0305	-117	-237	-400	...	...
Mrk 231	-237	-610	-1500	-386 (2)	6.66
IRAS 13120-5453	-195	-520	-1200	...	1.91
Mrk 273	-201	-495	-750	29 (2)	1.27
IRAS F14348-1447	-291:	-508	-900	...	15.2
IRAS F14378-3651	-219	-556	-1200	...	0.91
IRAS F15250+3608	189	-21	...	...	...
Arp 220	21	-153	-700	...	...
NGC 6240	-207	-544	-1200	-99 to -74 (1)	...
IRAS F17207-0014	51	-165	...	-298 to 27 (1)	...
IRAS F19297-0406	-231	-532	-1000	-413 to -114 (4)	...
IRAS 19542+1110	-93:	-489:	-700	...	...
IRAS F20551-4250	-381	-748	-1200	...	0.91
IRAS F22491-1808	99	3::	...	...	...
IRAS F23128-5919	...	...	...	...	...
IRAS F23365+3604	-243	-604	-1300	-384 ± 96 (4)	5.34

Note. — OH data adopted from V13. Negative velocities indicate blue-shifted absorption, positive values indicate red-shifted absorption. The uncertainties on the OH velocities are typically $50\,\mathrm{km\ s^{-1}}$, unless the value is followed by a colon (when the uncertainty is $50 - 150\,\mathrm{km\ s^{-1}}$), or a double colon (when the uncertainty is larger than $150\,\mathrm{km\ s^{-1}}$). v_{max}(abs) values have typical uncertainties of $200\,\mathrm{km\ s^{-1}}$. References for Na I D data (1): Rupke et al. (2005b) (2): Rupke et al. (2005a) (3): Rupke & Veilleux (2013a) (4): Martin (2005) OH masses are preliminary, final results will be published in González-Alfonso (in preparation).

and oversample set to 2 (resulting in $60\,\mathrm{km\,s^{-1}}$ sampling in the spectral direction).

We extracted both the point source corrected spectrum from the central spatial pixel (spaxel; one spaxel covers $(9.4'')^2$ on-sky) and the point source corrected sum of the central 9 spaxels. Although the central spaxel has the best signal to noise ratio, the [CII] emission might be slightly extended, or the telescope badly pointed, in which case the central 9 spaxels were used (Table 3).

The pointing was verified with a footprint plot, where a raster of the spectroscopic observations is overlaid on a PACS photometry map with higher spatial resolution. The source was not well centered on the central spaxel in four cases (F10565+2448, F12112+0305, 19542+1110, F23128-5919). In 5 other cases the final spectrum was extracted from the central 9 spaxels because the broad wings in the [CII] line profile differ from the central spaxel, hinting at slightly extended [CII] emission. Among these are the sources with double nuclei 08572+3915, separated by $6''$, and IRAS 23128-5919, separated by $4.5''$ (Surace et al. 1998; Zenner & Lenzen 1993). This choice does not affect the line fluxes much, because the central spaxel's flux is scaled to the (point source corrected) 9 spaxel flux, to account for the telescope Point Spread Function (PSF; $13''$ at 158 μm) and minor mispointings. The uncertainty in the line fluxes is 10% for flux densities > 1 Jy, but could be $\sim 30\%$ for any faint wings.

4. ANALYSIS AND RESULTS

More than half of all objects in our sample have broad wings in [CII] (14/22), as shown in the figures in Appendix A. Usually the wings appear both red-shifted and blue-shifted from the host galaxy, resulting in a symmetric line profile. This is expected if [CII] traces an outflow with a large opening angle, which looks rather like an expanding shell than a single blob. We will now assume that all OH outflows have a large opening angle, so that we can compare the blue-shifted velocity of the OH absorption with the full width at half maximum (FWHM) of the [CII] outflow.

4.1. Gaussian fits to the [CII] spectra

We have attempted to fit two Gaussian components (a narrow and a broad one) to the [CII] spectra. This should separate host galaxy emission from outflow emission. In most cases it is clear whether a broad component improves the fit or not. In case of doubt, we identify the best fit based on the reduced χ^2 value, i.e. we deem an outflow is present when the reduced χ^2 value of the two-component fit is lower than that of the one-component fit. We also visually inspect the fits to make sure that the second Gaussian fits the broad wings, not the central component. Figure 6 in Appendix A shows the fits overplotted on the [CII] line profiles, while Table 5 lists the Gaussian fits and their parameters.

The spectral resolution of PACS is $\sim 240\,\mathrm{km\,s^{-1}}$ at $158\,\mu$m. Any Gaussian fit with a FWHM

Table 3. [CII] observations

Name	OBSID	Extraction Spaxels	FWHM $\mathrm{km\,s^{-1}}$	1σ error $\mathrm{km\,s^{-1}}$	L_{outflow} $10^8 L_\odot$	M_{outflow} $10^8 M_\odot$
IRAS F05189-2524	1342219442	central	1213	412	0.68	1.45
IRAS 07251-0248	1342207825	central	-	502	-	-
IRAS F08572+3915	1342208952	3×3	1567	71	0.63	1.34
IRAS 09022-3615	1342209403	central	693	1	9.28	19.86
UGC 5101	1342208949	3×3	1158	394	0.6	1.28
IRAS F10565+2448	1342207788	3×3	882	1	2.01	4.29
IRAS F12112+0305	1342210832	3×3	-	161	-	-
Mrk 231	1342186811	central	940	8	1.48	3.18
IRAS 13120-5453	1342214629	central	1787	601	0.62	1.33
Mrk 273	1342207802	central	852	295	1.85	3.95
IRAS F14348-1447	1342224242	3×3	887	1	5.06	10.82
IRAS F14378-3651	1342204338	central	-	222	-	-
IRAS F15250+3608	1342213752	central	-	120	-	-
Arp 220	1342238930	central	-	173	-	-
NGC 6240	1342216623	3×3	934	29	8.23	17.62
IRAS F17207-0014	1342229693	central	-	177	-	-
IRAS F19297-0406	1342208891	central	1025	120	4.13	8.83
IRAS 19542+1110	1342208916	3×3	-	122	-	-
IRAS F20551-4250	1342208934	3×3	768	22	1.41	3.01
IRAS F22491-1808	1342211825	central	409	158	1.98	4.23
IRAS F23128-5919	1342210395	3×3	1027	18	2.27	4.87
IRAS F23365+3604	1342212515	central	-	106	-	-

Note. — [CII] observations: PACS obsid, the spaxels from which the spectrum was extracted, the average [CII] broad component FHWM after subtracting 240 $\mathrm{km\ s^{-1}}$ in quadrature (see Appendix A), the error as explained in Section 4.1, the luminosity of the [CII] broad component and the total neutral gas mass as described in Section 5.1. If no broad component is found, the error is the FHWM of the narrow component divided by 3. Outflow masses above $10^9 M_\odot$ should be regarded as upper limits because the outflow emission is contaminated by emission from the host galaxy.

below 240 km s^{-1} is therefore rejected. The PSF in PACS is not perfectly Gaussian, but it has no wings that could be confused with an outflow. In some objects, the fit to the continuum significantly affects the FWHM of the second component. Ideally, one would like to take the continuum far away from the systemic velocity of the host galaxy, in order to prevent the removal of broad wings. But the signal to noise ratio drops at (absolute) velocities above 1300 km s^{-1}. Faint wings extending to $>$ 1300 km s^{-1} can therefore not be reliably observed in the spectra. The fits have been done twice in order to estimate the error introduced in our method: once fitting the continuum close to the line, with the potential danger of removing the broad wings, and once fitting the continuum far away from the line, leaving plenty of room for the broad wings. We have adopted the average FWHM of these two fits to be the width of the [CII] broad component, and its difference to be the 3σ error. The difference can be very large in some cases: F05189-2524 and Mrk 273 are best fitted either with a second narrow Gaussian or with a broad component, while 07251-0248, 13120-5453, F14378-3651 and F22491-1808 can be fitted either with or without a broad component. In the first case, we take the FWHM of the broad component, to be consistent with the rest of our analysis. In the second case, we take the fit with the lowest reduced χ^2 value. The FWHM and error of the broad [CII] components are listed in Table 3.

There are some caveats in the analysis. Contamination by H_2O (158.3μm) may be present at 1080 km s^{-1}. It is not clear whether the bump around 1000 km s^{-1} in F19297-0406 is caused by red-shifted [CII] emission, or by H_2O emission. Two scenarios are fitted: one where the emission around 1000 km s^{-1} is a broad component, and another where this emission is included in the continuum fit. The average of the two FHWMs is used.

Another complication is that NGC 6240, Mrk 273 and UGC 5101 are not well described by a combination of 2 Gaussians. NGC 6240 is an early stage merger in which the two nuclei are well separated by 1.8″ in the I and r-band (Fried & Schulz 1983). Both nuclei are visible in the 3 mm continuum, but the CO(1-0) and CO(2-1) line intensities peak between the two nuclei (Tacconi et al. 1999; Feruglio et al. 2013b). The high spatial resolution maps in CO show that the line emission consists of several components. Also the [CII] line profile requires three components for a good fit. The [CII] line profile of Mrk 273 is irregular with a non-Gaussian shape. Cicone et al. (2014) observe a similar line profile in CO(1-0), and fit the central line with two Gaussians. We also fit two Gaussians to the central line in the [CII] profile, and add a third Gaussian for the broad component. The [CII] line profile in UGC 5101 suggests self-absorption or a 'double horn' profile as is typical for a disk seen edge-on. It could well arise from the molecular disk that is observed in CO(1-0) at velocities similar to the ones in the [CII] line profile (Genzel et al. 1998). The central line profile is well fitted by two Gaussians, and adding a third component slightly improves the overall fit.

4.2. Comparison with OH

All fourteen objects with broad [CII] wings either have an OH outflow (11), or inflow (1), with two exceptions: IRAS 23128-5919 clearly has wings in [CII], but the OH119 spectrum is too noisy to be fitted reliably. A faint P-Cygni profile may however be present with an estimated OH $v_{50} \sim -500\,\mathrm{km\,s^{-1}}$. We present the [CII] spectra and fits of this object in Appendix A but exclude it from our analysis. UGC 5101 has a marginally detected broad [CII] component, while OH $v_{50} = -9\,\mathrm{km\ s^{-1}}$. Faint high-velocity wings are however observed in the OH119 spectrum, which are better represented in this case by v_{84} and v_{max}. The object with an OH inflow is IRAS F22491-1808. Hubble Space Telescope observations of IRAS F22491-1808 reveal bright tails, which extend to 16 kpc from the center, and two nuclei separated by 2.5 kpc (Surace et al. 2000). We cannot exclude the possibility that the line profiles reflect tidal effects of a merger rather than an inflow. Inflows are excluded from the sample during the analysis.

A comparison of the OH blue-shifted velocities and broad [CII] FWHM is given in Figure 1, which shows the absolute values of the OH119 velocities (v_{50}, v_{84}, v_{max}) as function of the broad [CII] FWHM. The absolute value of the OH velocities is taken, because one can not distinguish an outflow from an inflow by observing only the [CII] wings. The three objects with an OH inflow ($v_{50} > 50\,\mathrm{km\,s^{-1}}$; F15250+3608, F17207-0014 and F22491-1808) are represented by small orange markers. Objects which do not require a broad component for a good fit to the [CII] spectrum are placed at $0\,\mathrm{km\ s^{-1}}$. We moreover added all three objects from Spoon et al. (2013) which have an outflow in both [CII] and OH119. Spoon et al. (2013) give the FWHM of the broad [CII] component and v_{max} of OH119. A blue-shifted and red-shifted component have been fitted to the OH119 spectra of 01003-2238 and 06035-7102, resulting in $v_{50} = -329$ and $-171\,\mathrm{km\ s^{-1}}$ respectively. 20100-4156 has a blended and broad absorption component, which we do not attempt to fit, so we have no v_{50} for this object. These objects are represented by purple markers in Figure 1, and are taken into account during the line fit (Equation 1) and the statistical analysis in Table 4.

Sixteen objects in our sample have OH outflows, defined in V13 to be the objects with OH $v_{50} < -50\,\mathrm{km\,s^{-1}}$. Eleven out of these objects also have [CII] broad wings, while five do not. Of these five objects, IRAS 23365+3604 is a real outlier; it has a high-velocity P-Cygni profile in OH but no trace of broad wings in [CII]. Although there is a small bump on the red side of the line, the width of this bump is smaller than the spectral resolution of PACS, and the feature is not considered to be real. IRAS 19542+1110 and IRAS 17208-0014, have low velocity OH outflows. The corresponding expected [CII] FWHM is too small for any outflow to be separable from the emission from the host galaxy. Finally, 07251-0248 and F14378-3651 may well have broad wings in [CII], but the reduced χ^2 value is smaller for the one-component fit.

The objects with a low-velocity OH outflow and no broad [CII] component are consistent with our hypothesis that broad [CII] traces OH outflows, but that a certain minimum velocity is required in order to distinguish emission of the outflow from that of the host galaxy. More qualitatively,

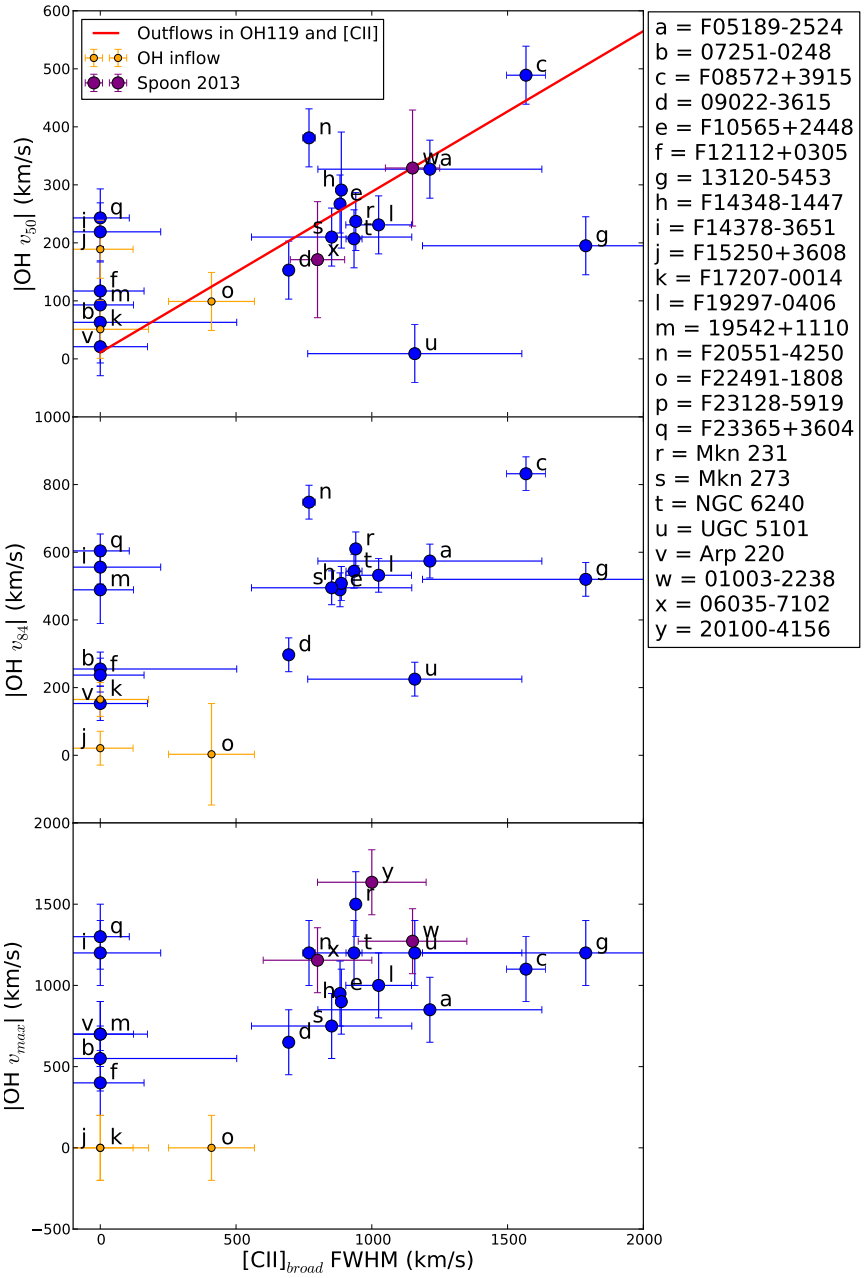

Fig. 1.— [CII] FWHM of the broad component plotted against the absolute value of the several OH velocities. Objects without a [CII] broad component are placed at $0\,\mathrm{km\,s^{-1}}$. The small orange markers represent objects with an inflow in OH119, having a red-shifted absorption ($v_{50} > 50\,\mathrm{km\,s^{-1}}$). Error bars for OH were adopted from V13, [CII] FWHM errors are listed in Table 3. Top panel: the red line is a weighted fit to all objects with detected outflows both in OH and C^+.

out of the eighteen objects which have detected OH119 velocities and no inflow (the blue points in Figure 1), fifteen are consistent with this hypothesis. Moreover, it is unlikely that a broad [CII] component traces an inflow: only one of the three objects with an OH inflow has a broad [CII] component, and it has a FWHM of only 409 km s^{-1}, which is low compared to the objects with outflows. These findings suggest that a broad [CII] component with a FWHM of > 500 km s^{-1} is a good indicator for the presence of an OH outflow.

We go one step further by comparing the actual outflow velocities. If C^+ traces an isotropic molecular outflow, a correlation is expected between the broad [CII] FHWM and the blue-shifted velocity of the OH absorption. [CII] seems to correlate with the absolute value of all OH velocities (Figure 1), in particular with v_{50}. A weighted least squares fit to |OH v_{50}|, for all objects that have an outflow detected both in OH and in C^+, results in:

$$|\mathrm{OH}\ v_{50}| = 11\,(\pm 96) + 0.28\,(\pm 0.10) \times \mathrm{CII}_{\mathrm{FWHM}} \quad (1)$$

where all velocities are given in km s^{-1}. Each observation is weigthed by $\max[\sigma_{\mathrm{OH}}, \sigma_{[\mathrm{CII}]}]^{-2}$, with σ_{OH} and $\sigma_{[\mathrm{CII}]}$ the errors in the OH velocity and broad [CII] FWHM respectively. Relation 1 is represented by the red line in the upper panel of Figure 1. The line goes through (0,0) within the uncertainties, as is expected when C^+ traces the OH outflow.

Is the apparent correlation in the upper panel of Figure 1 significant? We call a correlation statistically significant if the null hypothesis (the data points are randomly selected) can be rejected at a confidence level of 5%, using the Spearman rank coefficient and the Pearson correlation coefficient. When all objects with outflows in both OH and C^+ are included, only the Pearson correlation coefficient suggests a correlation. If IRAS 13120-5453 is removed from the sample, the correlation becomes tentative according to the Spearman rank coefficient and significant according to the Pearson correlation coefficient. Table 4 lists the correlation coefficients and confidence levels. The confidence levels for a two-tailed test have been retrieved from a table for low-number statistics, and are applicable to sample sizes of 4-30 data points (Wall & Jenkins 2003).

Although part of the lack of a strong correlation between the OH and C^+ velocities can be explained by the small sample, there is also intrinsic scatter in the relation. We assumed that each object has a large opening angle outflow, which is not necessarily the case. Moreover, there are uncertainties in the fits, in particular for objects with faint wings. And finally, C^+ and OH may trace different parts of the outflow. So although C^+ is in general a good tracer of the molecular outflow, significant deviations from the best fit in Equation 1 can remain in individual objects.

4.3. Correlation with AGN fraction and luminosity

In a previous analysis of 28 local ULIRGs, we found the OH v_{50} to correlate with the AGN fraction α_{agn} and AGN luminosity, although with significant scatter (V13). Part of the scatter is caused by uncertainty in the AGN luminosity, part again by our assumption of a spherical

Table 4. Correlation coefficients

Parameter (1)	N (2)	ρ_s (3)	P_ρ (4)	r (5)	P_r (6)	$P_r(N<30)$ (7)
CII_{broad} - $\lvert OHv_{50}\rvert$ (*)	13	0.34	...	0.36	0.23	0.05
CII_{broad} - $\lvert OHv_{84}\rvert$ (*)	11	0.47	0.2	0.39	0.24	...
CII_{broad} - $\lvert OHv_{50}\rvert$ (**)	12	0.55	0.1	0.75	0.01	0.02
CII_{broad} - $\lvert OHv_{84}\rvert$ (**)	10	0.59	0.1	0.65	0.04	0.05
CII_{broad} - α_{AGN}	14	0.4	0.2	0.27	0.35	...
CII_{broad} - L_{AGN}	14	0.06	...	-0.04	0.89	...
$\lvert OHv_{50}\rvert$- α_{AGN}	16	0.45	0.1	0.54	0.03	0.05
$\lvert OHv_{50}\rvert$ - L_{AGN}	16	0.29	...	0.29	0.28	...
CII_{broad} - $\lvert Nav_{50}\rvert$	8	0.48	...	0.74	0.04	0.05
OHv_{50} - Nav_{50}	10	0.7	0.05	0.74	0.01	0.02
OH mass - [CII] mass	8	0.61	0.2	0.9	0.01	0.01

Note. — (1) quantities considered for the test, (2) number of objects, (3) Spearman rank coefficient ρ_s, (4) confidence level for rejection of the null-hypothesis (there is no correlation between the 2 parameters) P_ρ, (5) Pearson correlation coefficient, (6) two-sided area after a Fisher transformation P_r, (7) confidence level for rejection of the null-hypothesis, using the t-value from the Pearson correlation coefficient. Note that P_ρ and $P_r(N<30)$ have been retrieved from a table for low-number statistics, and are applicable to sample sizes of 4-30 data points. If no value is given, the confidence levels are > 0.2 and not included in the tables for low-numbers statistics. * including all objects with a detected outflow in both OH and C^+. ** like * but excluding IRAS 13120-5453.

outflow with a large opening angle, and a constant coupling efficiency. Even in the absence of these uncertainties, an intrinsic scatter is expected due to different driving mechanisms and variable AGN luminosities. Nevertheless, we compare the AGN luminosity and AGN fraction with the broad [CII] FHWM and OH v_{50}, in order to see whether our subsample of V13 is large enough to reveal the same correlation as found earlier. Table 1 lists the AGN luminosity and fraction for our sources. α_{agn} has been calculated from f_{30}/f_{15} because these numbers are known for every object in the sample, and because this method shows the tightest relation with other methods to determine the AGN fraction (Veilleux et al. 2009). The error on the AGN fraction is typically 20%.

Figure 2 shows the relation of both the broad [CII] FHWM and OH v_{50} with α_{agn} for all objects with a detected outflow. There is no statistically significant correlation in any of the two plots, see Table 4. Figure 3 is similar to Figure 2, but now with the logarithm of the AGN luminosity on the x-axis. The uncertainties are taken to be 20% of the total luminosity. Also here, no statistically significant correlation is found with either the broad [CII] FWHM or OH v_{50}. We conclude that the current sample is too small, and covers too small a range in L_{AGN}, to find the same correlation as in V13.

4.4. Additional observations: Na I D

Ten objects in our sample have additional observations of blue-shifted Na I D $\lambda\lambda 5890, 5896$ absorption, observed by Rupke et al. (2005b), Rupke et al. (2005a), Rupke & Veilleux (2013a) and Martin (2005). Because Na I D observations are often spatially resolved, several velocities are available for each object. Table 2 lists the largest and smallest v_{50} values for the outflowing neutral gas, which were averaged for our analysis here. Figure 4 compares Na I D v_{50} to OH v_{50} and the broad [CII] FWHM. F08572+3915 has by far the highest velocity in OH and Na, and the second highest velocity in [CII]. Also for the other objects, Na I D v_{50} seems to correlate well with OH v_{50} (for all objects with a detection in both tracers), and with [CII] (for objects with a detection in Na I D and broad wings in [CII]). We give the Spearman rank coefficients and Pearson correlation coefficients in Table 4. Despite the small sample, the rejection levels suggest a significant correlation of the broad [CII] FWHM and OH v_{50} with Na v_{50}, which is however driven mostly by F08572+3915.

4.5. Additional observations: CO

Seven objects in our sample have CO(1-0) or CO(2-1) observations with sufficient S/N and velocity coverage to reveal broad wings. A comparison with [CII] is facilitated by CO and [CII] both appearing in emission and having similar critical densities. The critical density for the fine structure transition [CII] is $3.2 \times 10^3\,\mathrm{cm}^{-3}$ (using collision rates with atomic hydrogen at 100 K, Barinovs et al. (2005)). For CO(1-0) and CO(2-1), $n_{crit} = 2.1 \times 10^3\,\mathrm{cm}^{-3}$ and $n_{crit} = 2.2 \times 10^4\,\mathrm{cm}^{-3}$

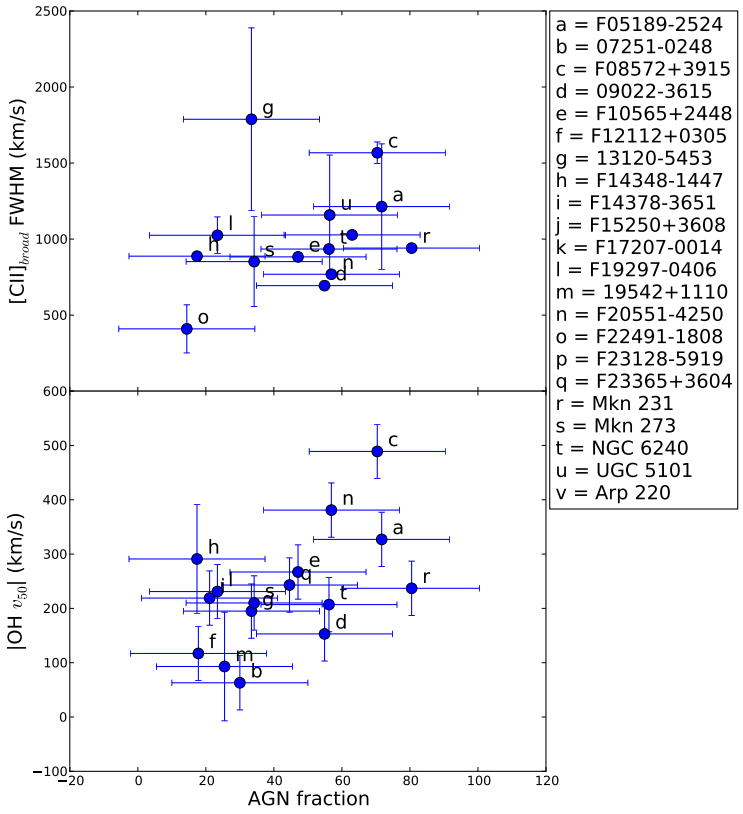

Fig. 2.— Upper panel: broad [CII] FWHM versus AGN fraction as listed in Table 1. Lower panel: OH v_{50} versus AGN fraction.

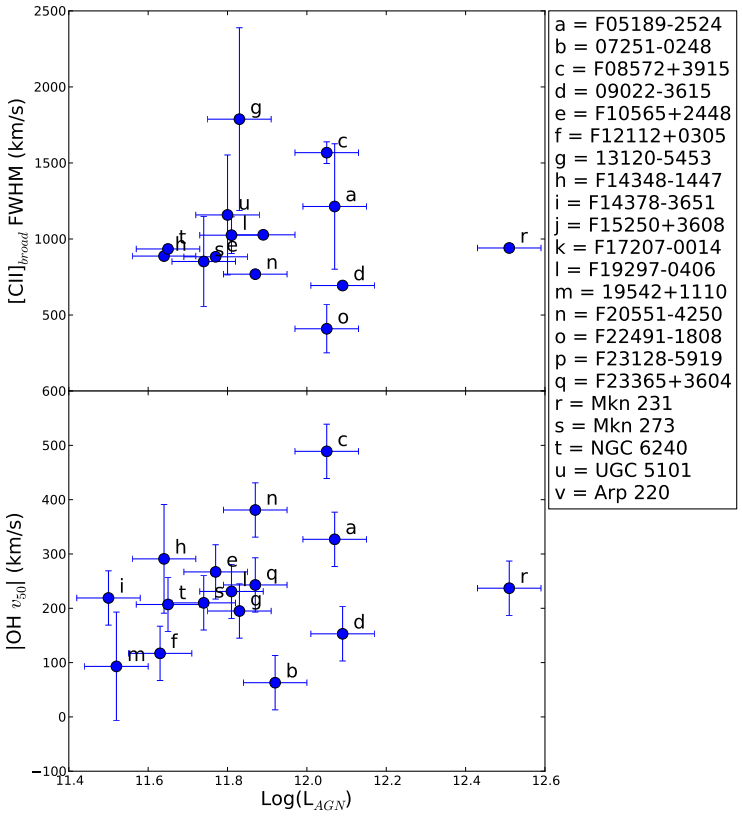

Fig. 3.— Upper panel: [CII] FWHM versus AGN luminosity as listed in Table 1. Lower panel: OH v_{50} versus AGN luminosity.

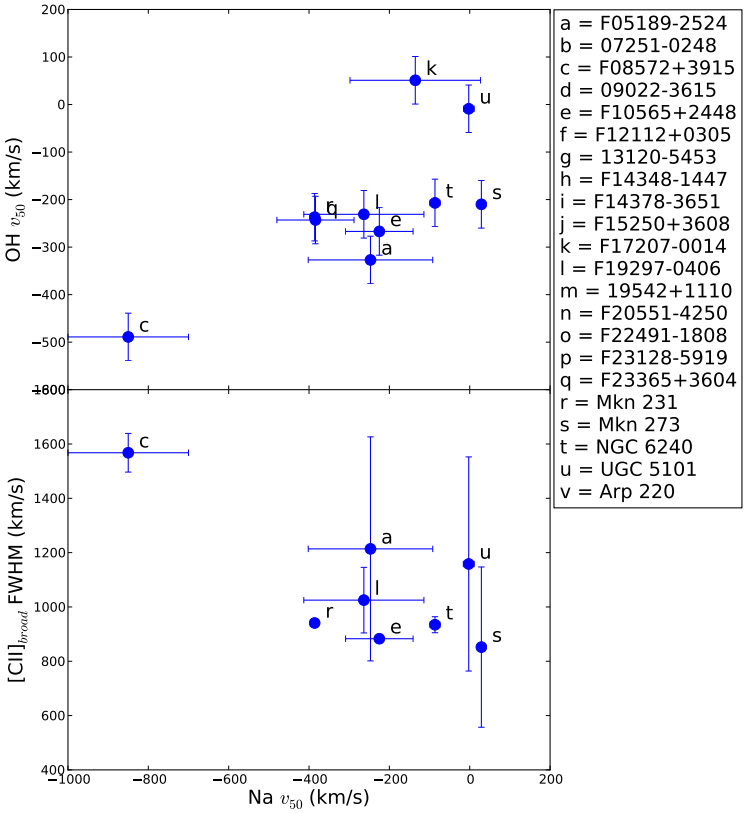

Fig. 4.— Na I D v_{50} compared to OH v_{50} (upper panel) and [CII] FHWM (lower panel). The upper panel shows objects with an OH inflow or outflow (we do not plot the absolute values here, in order to differentiate between inflows and outflows), the lower panel shows only objects with a detected [CII] outflow.

respectively (using collision rates with para-H_2 at 100 K, Yang et al. (2010)).

Feruglio et al. (2010) present CO(1-0) observations of Mrk 231. The line profile has been fitted with two components: a narrow one and a broad one with a FWHM of 870 $\mathrm{km\,s^{-1}}$ (compared to 971 $\mathrm{km\,s^{-1}}$ in [CII]). At higher spatial resolution, the source is slightly resolved at 1.1-1.3 kpc scale (Cicone et al. 2012). NGC 6240 has been observed in CO(1-0) by Feruglio et al. (2013a), who find a line profile extending from $-600\,\mathrm{km\,s^{-1}}$ to $+800\,\mathrm{km\,s^{-1}}$ (compared to $-1000\,\mathrm{km\,s^{-1}}$ to $+1500\,\mathrm{km\,s^{-1}}$ in [CII]).

Cicone et al. (2014) present CO(1-0) observations of F23365+3604, F10565+2448, Mrk 273 and F08572+3915 from our sample. F23365+3604 – with detected outflows in Na I D and OH but not in [CII] – clearly has broad CO wings, with flux densities of only 1% of the the peak emission. If the outflow is equally faint in the neutral gas traced by C^+, it would explain why no outflow was detected in [CII]: our PACS observations of [CII] do not reach the required sensitivity to detect such a faint component. The CO(1-0) profile for F10565+2448 has very bright wings, which is also the case in our [CII] spectra. F08572+3915 has the fastest CO outflow of the sample, with wings peaking around $-800\,\mathrm{km\,s^{-1}}$ and $+900\,\mathrm{km\,s^{-1}}$. In our sample, this object also has the highest outflow velocity in OH and Na I D, and the second highest velocity in [CII].

Recently, García-Burillo et al. (2015) published CO(2-1) spectra of IRAS F17207-0014, which revealed a complex line profile. After fitting it with 3 narrow line components, a residue is left between $-700\,\mathrm{km\,s^{-1}}$ and $-800\,\mathrm{km\,s^{-1}}$. There is however no obvious broad component, again in agreement with our findings from [CII].

The low-J CO and [CII] line profiles show many similarities, and we plan to provide a quantitative comparison in a future paper.

4.6. Uncertainties In The Fits And Alternative Velocity Determination

Some spectra in our sample have a [CII] line profile that can be fitted in different ways, resulting in large errors in the FWHM of the broad component. For example, 13120-5453 could either have an extremely broad component, or no broad component at all. The NGC 6240 line profile can be fitted with two or three components, which results in different values for the broad component FWHM. We therefore investigated alternatives. A more objective method is to take the velocities that enclose a certain fraction of the total (host galaxy + outflow) flux (the area-method). We applied this method at both 90% and 95% of the total flux, and found that 90% is a good compromise between being sensitive to faint emission and being dominated by noise. However, the velocities derived from this method do not correlate at all with the broad [CII] FWHM, the OH velocities, the Na I D velocities or the AGN fraction.

This discrepancy arises because the area-method depends strongly on the emission from the host galaxy, but the luminosity of the host galaxy does not correlate with that of the outflow. An

outflow may therefore not be caught when the central component is narrow, or its velocity may be overestimated if the central component is broad. Therefore, separating the host emission from the outflow emission seems necessary, even if this introduces large errors.

Another uncertainty lies in the decision to extract the spectrum from the central or the 3×3 spaxels. If all spectra are extracted from the central spaxel, the correlation between $[\mathrm{CII}]_{broad}$ FWHM and the OH velocities weakens a bit. Most importantly, the $[\mathrm{CII}]_{broad}$ FWHM of F08572+3915 decreases from $1586\,\mathrm{km\,s^{-1}}$ to $898\,\mathrm{km\,s^{-1}}$, which weakens the correlation between $[\mathrm{CII}]_{broad}$ FWHM and Na I D v_{50}. Otherwise, the results remain the same.

5. DISCUSSION

Studying a similar sample of 24 ULIRGs in OH119 and [CII], Spoon et al. (2013) and Farrah et al. (2013) only found 4 objects with broad wings in [CII]. In 3 objects the [CII] line width matches well with the line width of the blue-shifted OH absorption. The reason for finding only few [CII] broad components probably is, as the authors note themselves, that the observations do not have the required sensitivity to detect faint wings. The ULIRGs in their sample are fainter and at higher redshift ($z < 0.262$) than in our sample ($z < 0.1$).

5.1. Outflow Mass

The OH absorption only traces the molecular outflow along our line of sight to the FIR continuum. Calculation of the total outflow mass thus requires an assumption on the opening angle and geometry of the outflow. Moreover, the absorbed flux depends on the OH column density towards the source, on the covering factor of OH onto the FIR continuum, and on the FIR continuum intensity and spectral shape. A single OH transition is therefore not sufficient for mass determinations. We did however detect three or more OH transitions in some sources, and calculated the outflow mass for the 9 sources which 1) have detections of at least three out of the four transitions: OH119, OH79 ($^2\Pi_{1/2}\,1/2 \rightarrow {}^2\Pi_{3/2}\,3/2$), OH84 ($^2\Pi_{3/2}\,7/2 \rightarrow 5/2$) and OH65 ($^2\Pi_{3/2}\,9/2 \rightarrow 7/2$), 2) with clear P-Cygni profiles or broad wings, and 3) for which the spectra and fits look normal.

The model is described in González-Alfonso et al. (2014), and final results will be published in González-Alfonso (in preparation). A short description of the model is given here. Each object is described by the sum of three components: two outflow components (with different velocity, spatial extents and far-IR radiation sources) and one quiescent component. Free parameters of the model are: the inner- and outer- radius of the component, the dust temperature, the continuum optical depth at $100\,\mu$m, the gas velocity at R_{in}, the gas velocity at R_{out}, the OH column density, the impact parameter (giving the on-sky spatial extend of the outflow) and the scaling factor (related to the covering factor of OH with respect to FIR continuum). Each component is divided in at least 20 concentric shells. The statistical-equilibrium populations are calculated in each shell, and

the emerging line shapes are calculated and convolved with the PACS spectral resolution. These modelled line profiles are then compared to the three or more available spectra in OH, and the best fit is used. The mass is derived from the outflow components only. Figure 5 compares these outflow masses based on OH absorption with those based on [CII] emission.

The mass of the neutral atomic outflow was derived from the [CII] broad component using the cooling law as described in the appendix of Tielens & Hollenbach (1985), and assuming that [CII] is optically thin:

$$n^2\Lambda = \frac{g_u/g_l \exp[-h\nu_{ul}/kT]}{1 + n_{cr}/n + g_u/g_l \exp[-h\nu_{ul}/kT]}\, \chi_{C^+} n A_{ul} h\nu_{ul} \quad (2)$$

This equation describes the cooling of the interstellar medium (ISM) per unit volume due to line emission ($[n^2\Lambda] = \mathrm{J\,s^{-1}\,cm^{-3}}$). The ratio of the statistical weights of the upper and lower level $g_u/g_l = 2$, $h\nu_{ul}/k = 91\,\mathrm{K}$, the critical density $n_{cr} = 3.2 \times 10^3\,\mathrm{cm^{-3}}$ in neutral medium (Barinovs et al. 2005), the abundance $\chi_{C^+} = 1.4 \times 10^{-4}$, the Einstein coefficient for spontaneous emission $A_{ul} = 2.4 \times 10^{-6}\,\mathrm{s^{-1}}$, and the frequency $\nu_{ul} = 1.9 \times 10^{12}\,\mathrm{Hz}$. Filling in these constants results in the following equation:

$$\frac{M_N}{M_\odot} = 1.34 \frac{L_{\mathrm{CII}}}{L_\odot} \times \frac{1 + n_{cr}/n + 2\exp[-91\mathrm{K}/T]}{2\exp[-91\mathrm{K}/T]} \quad (3)$$

where we assumed that 25% of the mass is in helium, and that all broad [CII] emission arises from atomic gas.

In order to derive the density and temperature we need either a CO line SED or FIR SED plus density tracers, but these observations are not available for the outflows. Instead, we will use $n = 10^5\,\mathrm{cm^{-3}}$ and $T = 100\,\mathrm{K}$, which should be typical conditions in ULIRGs (Sanders & Mirabel 1996; Veilleux et al. 2009; Mashian et al. 2015). The fraction in Equation 3 becomes 2.28. This number is quite conservative, as it is less than twice as large as the factor retrieved for infinitely large density and temperature (1.5). With an uncertainty of 50% due to unknown temperature and density and a 30% flux calibration error, we adopt a total error of 80%. Table 3 lists the luminosities of the broad components and the derived total neutral gas masses. These masses are probably too high for NGC 6240, F14348-1447 and 09022-3615 ($M > 10^9 M_\odot$), because the outflow emission could not be separated well from the host galaxy emission.

There appears to be a tentative 1:1 relation between the derived outflow masses from OH and [CII], albeit within the large uncertainties (Figure 5). Together with the observed trend between the broad [CII] FWHM and OH $v50$, this supports our hypothesis that a broad [CII] component is a plausible tracer of molecular outflows in galaxies. The mass has been calculated from OH by adopting an abundance of 2.5×10^{-6} relative to H nuclei and including a factor of 1.4 due to Helium. Both derivations should therefore result in similar masses if the same amount of particles is involved. An exact 1:1 relation is not necessarily expected. OH absorption arises predominantly from the molecular gas while C^+ emission arises from atomic and molecular gas. Some overlap between the two tracers is expected, but it is not known how much. Yet, within these uncertainties, the mass

derived from the luminosity of the broad [CII] component seems to agree well with the outflow mass derived from OH. The relation is significant according to the Pearson correlation coefficient, but not if the Spearman rank coefficient is used (Table 4). However, we stress here that the OH masses are preliminary results, and that the correlation is driven by the large mass in IRAS F14348-1447 ($1 - 2 \times 10^9\,M_\odot$).

5.2. Origin of the [CII] broad wings

The P-Cygni profiles and blue-shifted absorptions in OH are clear signs of outflowing gas. Broad wings in [CII] on the other hand, can be caused by outflows, inflows, turbulence, or a high velocity rotation disk. However, the OH spectra have shown that the ULIRGs in our sample contain molecular outflows more often than inflows (16 outflows versus 3 inflows). Furthermore, all outflow masses derived from OH and [CII] lie along a 1:1 relation within the uncertainties. Adding to that the trend of the broad [CII] FWHM with OH v_{50}, leads us to the conclusion that [CII] traces and is likely entrained in the OH outflow.

This does not mean that [CII] broad wings exclusively trace molecular outflows: the broad [CII] FWHM also shows a trend with Na I D blue-shifted velocity (Figure 4, Table 4), suggesting an origin in atomic gas. V13 already found a correlation between Na I D v_{50} and OH v_{50}, showing that the atomic and molecular outflow are mixed or that OH absorption arises mostly from the atomic gas.

Multi-phase outflows have been observed before, although the connection between the different phases is not always clear (Shih & Rupke 2010; Westmoquette et al. 2013; Kreckel et al. 2014; Morganti et al. 2015). Gas phases with similar outflow velocities can be explained by gas mixing. For example, Contursi et al. (2013) explain the similar velocities of [OIII] $\lambda\,88\mu$m, [OI] $\lambda\,63\,\mu$m and $\lambda\,145\,\mu$m, [CII], and CO(1-0) in M82, by assuming that the outflow consists of small molecular cloudlets which are ionized on the outside, but remain molecular inside. In this way, the different phases do not only have the same velocity, but are also cospatial. Spatially resolved observations of the outflows would therefore help to explain the connection between the gas phases.

Rupke & Veilleux (2013b) present spatially resolved IFU observations of Na I D and H α of the following ULIRGs in our sample: F08572+3915, F10565+2448, Mrk 231, Mrk 273 and F17207-0014 (F17207-0014 only has Na I D detected). All of them have extended outflows with a radius ≥ 1 kpc. These kpc-scales may be hard to unite with the scale of the OH absorption. PACS did not resolve the OH absorption, but there are several indications that the absorption arises from scales ≤ 1 kpc:

- Using the model as described in Section 5.1, Sturm et al. (2011) find inner radii of 100-200 pc for the OH outflow for five objects in our sample, and outer radii of a few hundred pc.
- Spoon et al. (2013) use the anti-correlation between OH119 equivalent width and the silicate strength to argue that the OH119 absorption arises in the buried nucleus.

- Rupke & Veilleux (2013a) present spatially resolved observations of the H_2 outflow in F08572+3915 (NW) at 400 pc. The outflow velocities correspond well with those observed in OH.

There is however a bias in the determination of the spatial scale at which OH absorption takes place, because a bright FIR continuum is needed. If this continuum has a smaller spatial extent than the OH outflow, a significant part of the OH outflow will not be illuminated. Lutz et al. (2015) recently published the Herschel/PACS FIR radii at 70 μm for our objects, and provided us with the radii at 100 μm (private communication). These radii range from below 0.5 kpc to 2.8 kpc, and are typically around 1 kpc for our sample. The OH outflow could therefore be more extended than what we infer from the PACS observations.

If the outflow is located at a kpc from the nucleus, would it be able to escape the gravitational potential of the galaxy? Based on the widths of the narrow components of the [CII] line profile (deconvolved with the spectral PACS PSF), we derive a typical dynamical mass of $10^{10}\,M_{\odot}$. We do not take any inclination effects into account for the disk-dominated objects. For a central mass of $10^{10}\,M_{\odot}$, the escape velocity is $\sim 300\,\mathrm{km\ s^{-1}}$, which is reached by most C^+ outflows. Part of the gas could therefore escape the central few kiloparsec of the galaxy, although it may not escape the halo.

6. SUMMARY AND CONCLUSION

We address the question of whether [CII] at 158 μm is a good tracer of outflows in general, and molecular outflows in particular. The sample consists of 22 local and bright ULIRGs, of which 16 objects have molecular outflows as traced by OH 119 μm absorption at velocities $< -50\,\mathrm{km\,s^{-1}}$. Because [CII] appears in emission, any isotropic and spatially unresolved outflow becomes visible as broad wings in the line profile. We fitted the [CII] line profiles with two Gaussians, in order to separate host emission from outflow emission, and use the FWHM of the broad component to estimate the outflow velocity. The main results are:

1. Fourteen objects in our sample show broad [CII] wings. Eleven of these objects contain an OH outflow, one contains an inflow, one object has a noisy OH spectrum and is removed from the analysis, and one has a faint outflow which is not traced by OH v_{50} (the median velocity of the blue-shifted absorption). If all objects with an outflow in [CII] and OH119 are taken into account, the FWHM of the broad [CII] component shows a tentative correlation with OH v_{50} and v_{84}.

2. Observations of Na I D are available for 10 sources in the sample. The FWHM of the broad [CII] component shows a trend with the Na I D v_{50}. This is not surprising, since Na I D v_{50} was already found to correlate with the OH v_{50} in V13. [CII] may thus trace both the molecular and atomic gas in the neutral outflow, and part of the OH absorption could arise from the atomic gas as well.

3. The broad [CII] FWHM does not show a correlation with either the AGN luminosity or the AGN fraction. This might be caused by a combination of large uncertainties in the AGN luminosity and fraction, intrinsic scatter, and the small sample: no correlation is found between OH v_{50} and AGN fraction or luminosity either, although such a correlation was found when using a larger sample.

4. Preliminary estimates of the molecular outflow mass, based on at least 3 OH line profiles, are given for 9 objects. These masses lie roughly on a 1:1 relation with the outflow mass derived from the broad [CII] component, and can be up to $10^9\,M_\odot$. This shows that both OH and C^+ trace the same (or similar fractions of the) massive outflows observed in ULIRGs.

5. We conclude that the broad [CII] wings are a good tracer of both the molecular and atomic phases of the outflow, and that the outflow mass based on [CII] is a good estimate of the molecular outflow mass.

We wish to thank Steve Hailey-Dunsheath for discussing equation 3 with us, and Henrik Spoon for providing us with the OH119 spectra of objects in his sample. We also thank the referee for his/her helpful comments. J.F. acknowledges support from the NHSC/ JPL subcontracts 139807 and 1456609; Basic research in IR astronomy at NRL is funded by the US-ONR. E.G-A is a Research Associate at the Harvard-Smithsonian Center for Astrophysics, and thanks the Spanish Ministerio de Economía y Competitividad for support under project FIS2012-39162-C06-01, and NASA grant ADAP NNX15AE56G. A.S. thanks the DFG for support via German-Israeli Project Cooperation grant STE1869/1-1.GE625/15-1. S.V. acknowledges support by NASA through Herschel contracts 1427277 and 1454738. A.V. acknowledges support from the Leverhulme Trust in the form of a Research Fellowship. PACS has been developed by a consortium of institutes led by MPE (Germany) and including UVIE (Austria); KU Leuven, CSL, IMEC (Belgium); CEA, LAM (France); MPIA (Germany); INAF-IFSI/OAA/OAP/OAT, LENS, SISSA (Italy); IAC (Spain). This development has been supported by the funding agencies BMVIT (Austria), ESA-PRODEX (Belgium), CEA/CNES (France), DLR (Germany), ASI/INAF (Italy), and CICYT/MCYT (Spain).

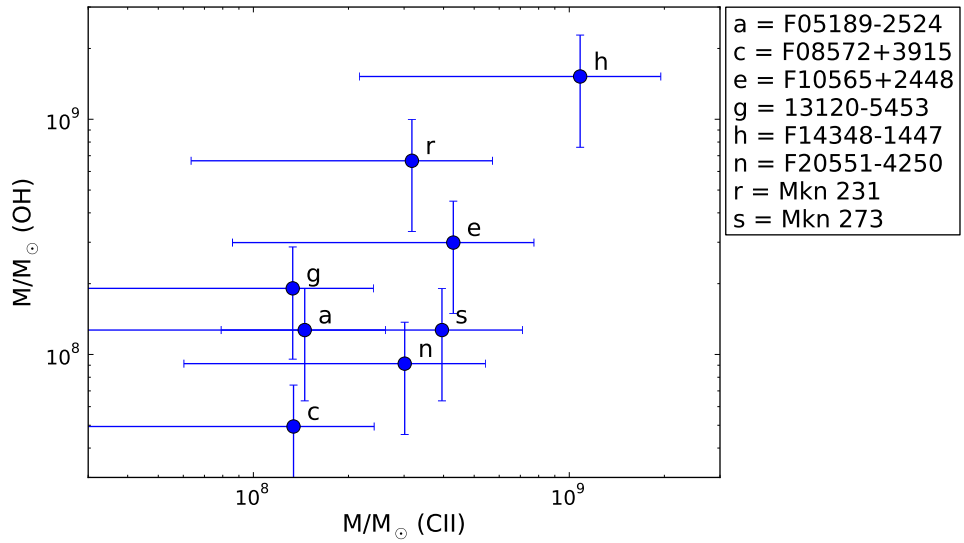

Fig. 5.— Total molecular outflow mass based on OH line modelling by González-Alfonso (in preparation) on the y-axis, and atomic outflow mass based on the luminosity of the [CII] broad component on the x-axis.

REFERENCES

Alexander, D.M., Swinbank, A.M., Smail, I., McDermid, R., & Nesvadba, N.P.H., 2010, MNRAS, 402, 2211

Arribas, S., Colina, L., Bellocchi, E., Maiolino, R., & Villar-Martín, M., 2014, A&A, 568, A14

Banerji, M., Chapman, S.C., Smail, I., et al., 2011, MNRAS, 418, 1071

Barinovs, Ğ., van Hemert, M.C., Krems, R., & Dalgarno, A., 2005, ApJ, 620, 537

Cano-Díaz, M., Maiolino, R., Marconi, A., et al., 2012, A&A, 537, L8

Cecil, G., Bland, J., & Tully, R.B., 1990, ApJ, 355, 70

Cicone, C., Feruglio, C., Maiolino, R., et al., 2012, A&A, 543, A99

Cicone, C., Maiolino, R., Gallerani, S., et al., 2015, A&A, 574, A14

Cicone, C., Maiolino, R., Sturm, E., et al., 2014, A&A, 562, A21

Cole, S., 1991, ApJ, 367, 45

Contursi, A., Poglitsch, A., Grácia Carpio, J., et al., 2013, A&A, 549, A118

Diamond-Stanic, A.M., Moustakas, J., Tremonti, C.A., et al., 2012, ApJ, 755, L26

Efstathiou, G., 2000, MNRAS, 317, 697

Fabian, A.C., 2012, ARA&A, 50, 455

Farrah, D., Lebouteiller, V., Spoon, H.W.W., et al., 2013, ApJ, 776, 38

Feruglio, C., Fiore, F., Maiolino, R., et al., 2013a, A&A, 549, A51

Feruglio, C., Fiore, F., Piconcelli, E., et al., 2013b, A&A, 558, A87

Feruglio, C., Maiolino, R., Piconcelli, E., et al., 2010, A&A, 518, L155

Fischer, J., Sturm, E., González-Alfonso, E., et al., 2010, A&A, 518, L41

Förster Schreiber, N.M., Genzel, R., Newman, S.F., et al., 2014, ApJ, 787, 38

Fried, J.W. & Schulz, H., 1983, A&A, 118, 166

García-Burillo, S., Combes, F., Usero, A., et al., 2015, A&A, 580, A35

Genzel, R., Förster Schreiber, N.M., Rosario, D., et al., 2014, ApJ, 796, 7

Genzel, R., Lutz, D., Sturm, E., et al., 1998, ApJ, 498, 579

González-Alfonso, E., Fischer, J., Graciá-Carpio, J., et al., 2014, A&A, 561, A27

Harrison, C.M., Alexander, D.M., Mullaney, J.R., & Swinbank, A.M., 2014, MNRAS, 441, 3306

Harrison, C.M., Alexander, D.M., Swinbank, A.M., et al., 2012, MNRAS, 426, 1073

Heckman, T.M., Alexandroff, R.M., Borthakur, S., Overzier, R., & Leitherer, C., 2015, ApJ, 809, 147

Heckman, T.M. & Best, P.N., 2014, ARA&A, 52, 589

Heckman, T.M., Borthakur, S., Overzier, R., et al., 2011, ApJ, 730, 5

Hopkins, P.F., Quataert, E., & Murray, N., 2012, MNRAS, 421, 3522

Kreckel, K., Armus, L., Groves, B., et al., 2014, ApJ, 790, 26

Lutz, D., Berta, S., Contursi, A., et al., 2015, ArXiv e-prints

Maiolino, R., Gallerani, S., Neri, R., et al., 2012, MNRAS, 425, L66

Marlowe, A.T., Heckman, T.M., Wyse, R.F.G., & Schommer, R., 1995, ApJ, 438, 563

Martin, C.L., 1998, ApJ, 506, 222

Martin, C.L., 2005, ApJ, 621, 227

Mashian, N., Sturm, E., Sternberg, A., et al., 2015, ApJ, 802, 81

Meijerink, R. & Spaans, M., 2005, A&A, 436, 397

Morganti, R., Oosterloo, T., Oonk, J.B.R., Frieswijk, W., & Tadhunter, C., 2015, A&A, 580, A1

Morganti, R., Tadhunter, C.N., & Oosterloo, T.A., 2005, A&A, 444, L9

Murray, N., Quataert, E., & Thompson, T.A., 2005, ApJ, 618, 569

Nesvadba, N.P.H., Lehnert, M.D., De Breuck, C., Gilbert, A.M., & van Breugel, W., 2008, A&A, 491, 407

Nesvadba, N.P.H., Polletta, M., Lehnert, M.D., et al., 2011, MNRAS, 415, 2359

Pilbratt, G.L., Riedinger, J.R., Passvogel, T., et al., 2010, A&A, 518, L1

Pineda, J.L., Langer, W.D., Velusamy, T., & Goldsmith, P.F., 2013, A&A, 554, A103

Poglitsch, A., Waelkens, C., Geis, N., et al., 2010, A&A, 518, L2

Rand, R.J., 1996, ApJ, 462, 712

Riechers, D.A., Carilli, C.L., Capak, P.L., et al., 2014, ApJ, 796, 84

Rupke, D.S., Veilleux, S., & Sanders, D.B., 2005a, ApJ, 632, 751

Rupke, D.S., Veilleux, S., & Sanders, D.B., 2005b, ApJS, 160, 87

Rupke, D.S.N. & Veilleux, S., 2013a, ApJ, 775, L15

Rupke, D.S.N. & Veilleux, S., 2013b, ApJ, 768, 75

Sakamoto, K., Aalto, S., Wilner, D.J., et al., 2009, ApJ, 700, L104

Sales, L.V., Navarro, J.F., Schaye, J., et al., 2010, MNRAS, 409, 1541

Sanders, D.B., Mazzarella, J.M., Kim, D.C., Surace, J.A., & Soifer, B.T., 2003, AJ, 126, 1607

Sanders, D.B. & Mirabel, I.F., 1996, ARA&A, 34, 749

Shih, H.Y. & Rupke, D.S.N., 2010, ApJ, 724, 1430

Silk, J., 2011, in C. Carignan, F. Combes, & K.C. Freeman, editors, *IAU Symposium*, volume 277 of *IAU Symposium*, 273–281

Spoon, H.W.W., Farrah, D., Lebouteiller, V., et al., 2013, ApJ, 775, 127

Spoon, H.W.W. & Holt, J., 2009, ApJ, 702, L42

Sturm, E., González-Alfonso, E., Veilleux, S., et al., 2011, ApJ, 733, L16

Surace, J.A., Sanders, D.B., & Evans, A.S., 2000, ApJ, 529, 170

Surace, J.A., Sanders, D.B., Vacca, W.D., Veilleux, S., & Mazzarella, J.M., 1998, ApJ, 492, 116

Tacconi, L.J., Genzel, R., Tecza, M., et al., 1999, ApJ, 524, 732

Tielens, A.G.G.M. & Hollenbach, D., 1985, ApJ, 291, 722

Veilleux, S., Meléndez, M., Sturm, E., et al., 2013, ApJ, 776, 27

Veilleux, S., Rupke, D.S.N., Kim, D.C., et al., 2009, ApJS, 182, 628

Vogelsberger, M., Genel, S., Sijacki, D., et al., 2013, MNRAS, 436, 3031

Wall, J.V. & Jenkins, C.R., 2003, *Practical Statistics for Astronomers*

Weiner, B.J., Coil, A.L., Prochaska, J.X., et al., 2009, ApJ, 692, 187

Westmoquette, M.S., Clements, D.L., Bendo, G.J., & Khan, S.A., 2012, MNRAS, 424, 416

Westmoquette, M.S., Smith, L.J., Gallagher, J.S., & Walter, F., 2013, MNRAS, 428, 1743

Yang, B., Stancil, P.C., Balakrishnan, N., & Forrey, R.C., 2010, ApJ, 718, 1062

Zenner, S. & Lenzen, R., 1993, A&AS, 101, 363

7. APPENDIX A: GAUSSIAN FITS

Figure 6 shows the [CII] spectra for each source in our sample. Each subfigure lists the FHWM of the broad component and the reduced χ^2 value for the fit. The fit has been done to the normal (linearly scaled) flux density, but here the y-axis is shown in a logarithmic scale, to increase the visibility of the low signal wings. The residual plot below each figure is shown in linear scale. Shaded areas mark the range that was chosen for the continuum fit. The [CII] spectra for each source in our sample are plotted twice, in order estimate the error on the FWHM of the broad component. In the first subfigure, the continuum was fitted close to the line, at good signal to noise, but potentially removing broad lines and minimizing the FWHM of the broad component. In the second figure, the continuum was fitted far away from the line, at the edges where the signal to noise ratio was low, but leaving plenty of room for a broad component. Because the spectra are only fully covered from $-1300\,\mathrm{km\ s^{-1}}$ to $+1300\,\mathrm{km\ s^{-1}}$, and the part outside this region has been scanned less frequently, the noise steadily increases at velocities $< -1300\,\mathrm{km\ s^{-1}}$ and $> 1300\,\mathrm{km\ s^{-1}}$. We therefore avoid fitting the continuum in high-velocity regions with sudden peaks and dips in the spectrum. After continuum subtraction, we attempted to fit two Gaussians (and in exceptional cases three Gaussians) to the line profile. Table 5 contains all the parameters of the Gaussian fits.

This preprint was prepared with the AAS LaTeX macros v5.2.

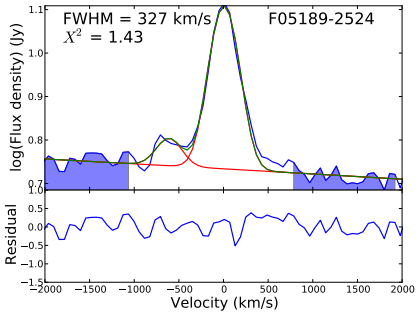
FWHM = 327 km/s
X^2 = 1.43
F05189-2524
log(Flux density) (Jy)
Residual
Velocity (km/s)

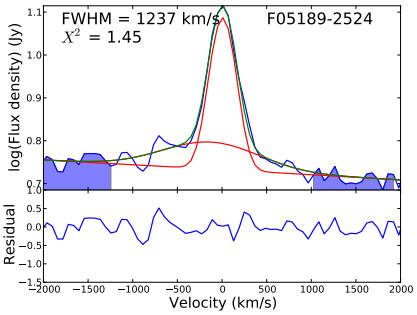
FWHM = 1237 km/s
X^2 = 1.45
F05189-2524
log(Flux density) (Jy)
Residual
Velocity (km/s)

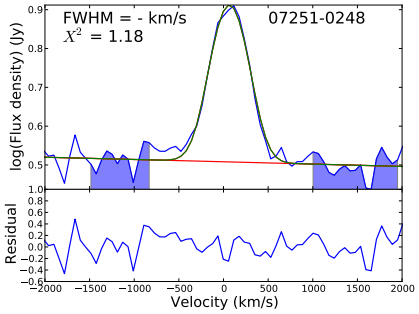
FWHM = - km/s
X^2 = 1.18
07251-0248
log(Flux density) (Jy)
Residual
Velocity (km/s)

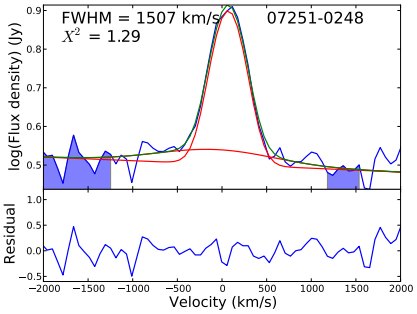
FWHM = 1507 km/s
X^2 = 1.29
07251-0248
log(Flux density) (Jy)
Residual
Velocity (km/s)

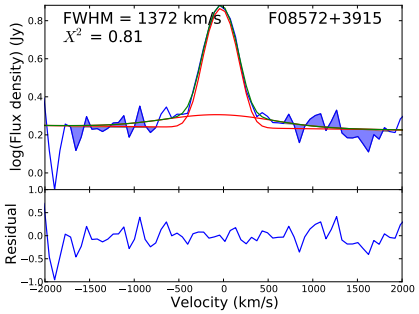
FWHM = 1372 km/s
X^2 = 0.81
F08572+3915
log(Flux density) (Jy)
Residual
Velocity (km/s)

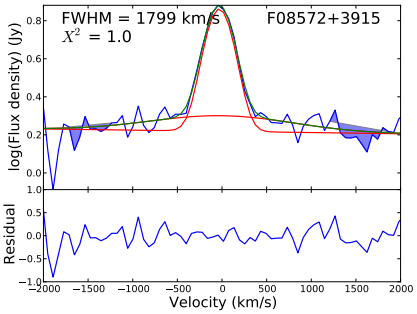
FWHM = 1799 km/s
X^2 = 1.0
F08572+3915
log(Flux density) (Jy)
Residual
Velocity (km/s)

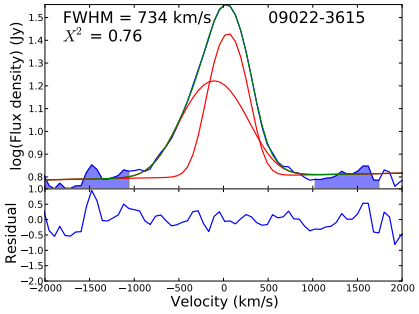
FWHM = 734 km/s
X^2 = 0.76
09022-3615
log(Flux density) (Jy)
Residual
Velocity (km/s)

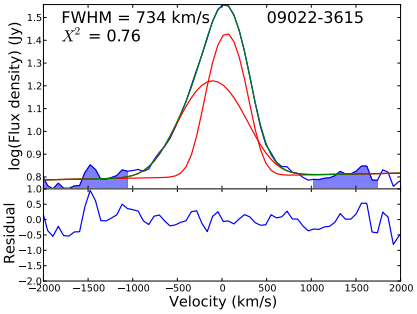
FWHM = 734 km/s
X^2 = 0.76
09022-3615
log(Flux density) (Jy)
Residual
Velocity (km/s)

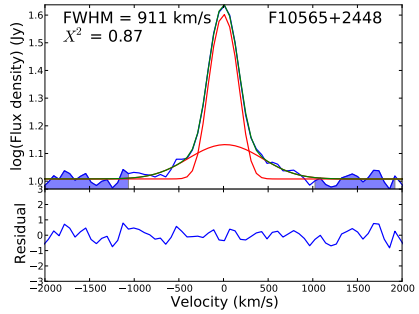
FWHM = 911 km/s
X^2 = 0.87
F10565+2448
log(Flux density) (Jy)
Residual
Velocity (km/s)

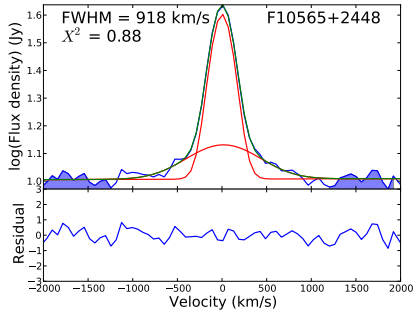
FWHM = 918 km/s
X^2 = 0.88
F10565+2448
log(Flux density) (Jy)
Residual
Velocity (km/s)

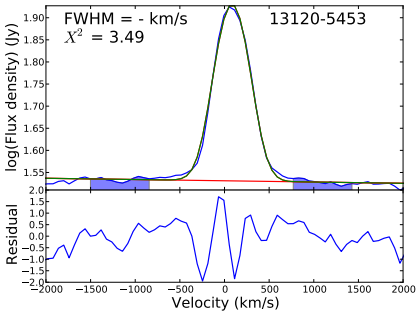
FWHM = - km/s
X^2 = 3.49
13120-5453
log(Flux density) (Jy)
Residual
Velocity (km/s)

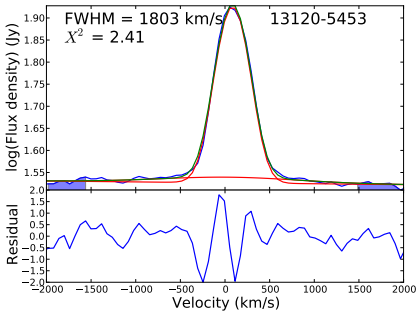
FWHM = 1803 km/s
X^2 = 2.41
13120-5453
log(Flux density) (Jy)
Residual
Velocity (km/s)

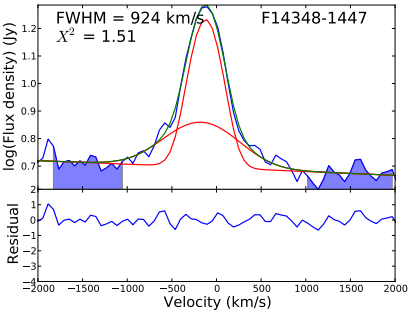
FWHM = 924 km/s
X^2 = 1.51
F14348-1447
log(Flux density) (Jy)
Residual
Velocity (km/s)

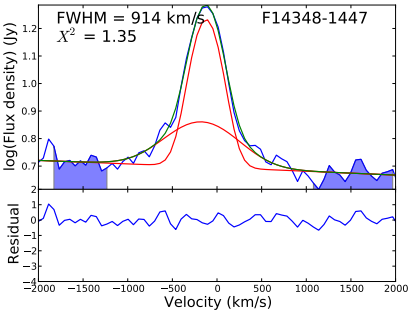
FWHM = 914 km/s
X^2 = 1.35
F14348-1447
log(Flux density) (Jy)
Residual
Velocity (km/s)

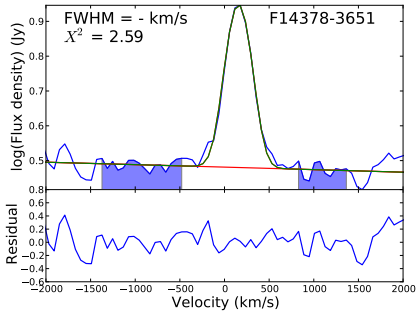
FWHM = - km/s
X^2 = 2.59
F14378-3651
log(Flux density) (Jy)
Residual
Velocity (km/s)

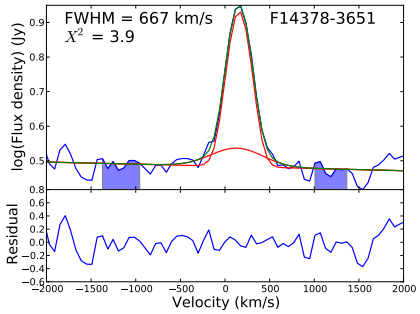
FWHM = 667 km/s
X^2 = 3.9
F14378-3651
log(Flux density) (Jy)
Residual
Velocity (km/s)

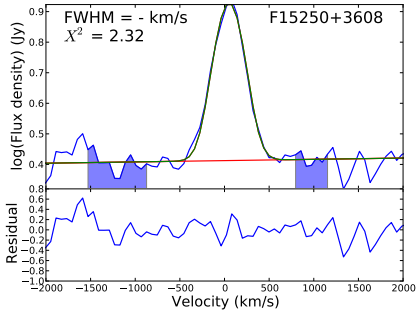
FWHM = - km/s
X^2 = 2.32
F15250+3608
log(Flux density) (Jy)
Residual
Velocity (km/s)

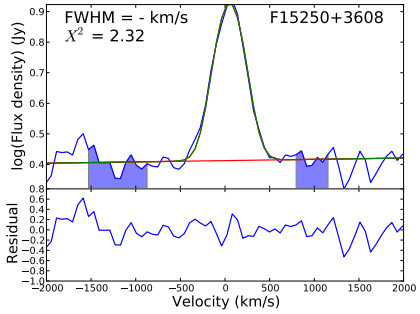
FWHM = - km/s
X^2 = 2.32
F15250+3608
log(Flux density) (Jy)
Residual
Velocity (km/s)

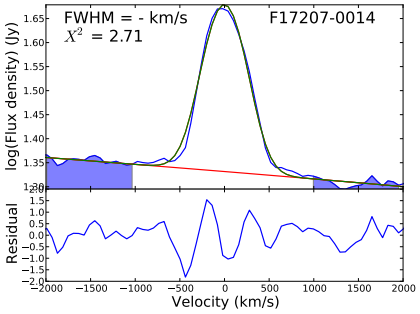
FWHM = - km/s
X^2 = 2.71
F17207-0014
log(Flux density) (Jy)
Residual
Velocity (km/s)

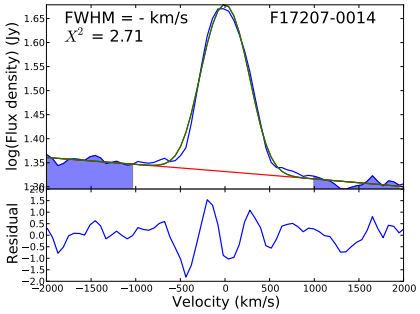
FWHM = - km/s
X^2 = 2.71
F17207-0014
log(Flux density) (Jy)
Residual
Velocity (km/s)

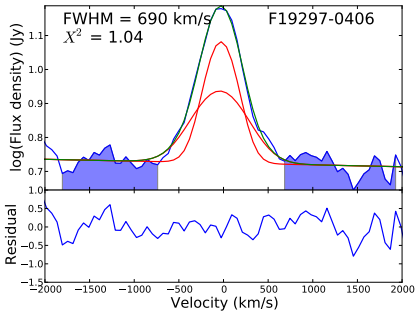
FWHM = 690 km/s
X^2 = 1.04
F19297-0406
log(Flux density) (Jy)
Residual
Velocity (km/s)

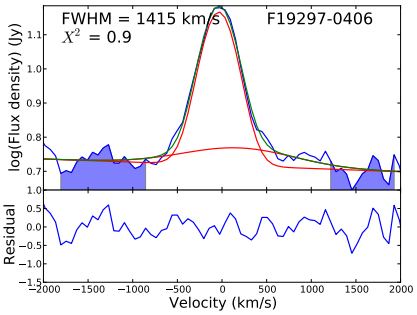
FWHM = 1415 km/s
X^2 = 0.9
F19297-0406
log(Flux density) (Jy)
Residual
Velocity (km/s)

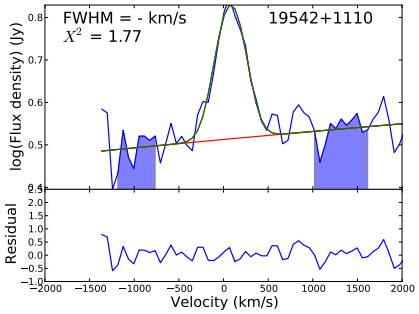
FWHM = - km/s
X^2 = 1.77
19542+1110
log(Flux density) (Jy)
Residual
Velocity (km/s)

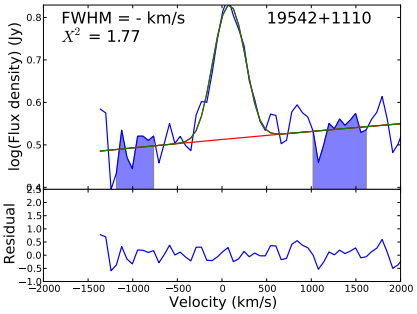
FWHM = - km/s
X^2 = 1.77
19542+1110
log(Flux density) (Jy)
Residual
Velocity (km/s)

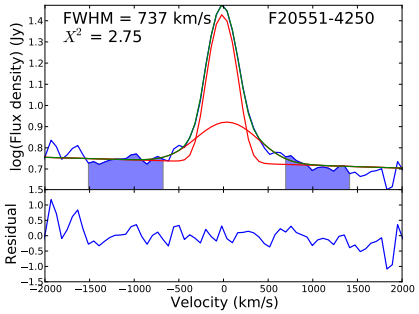
FWHM = 737 km/s
X^2 = 2.75
F20551-4250
log(Flux density) (Jy)
Residual
Velocity (km/s)

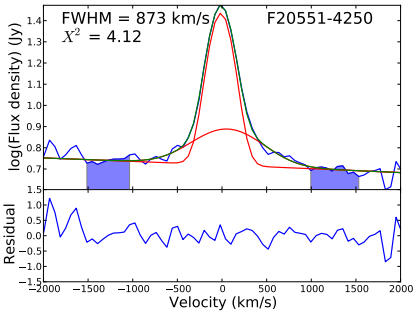
FWHM = 873 km/s
X^2 = 4.12
F20551-4250
log(Flux density) (Jy)
Residual
Velocity (km/s)

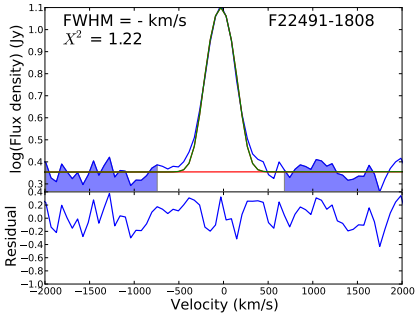
FWHM = - km/s
X^2 = 1.22
F22491-1808
log(Flux density) (Jy)
Residual
Velocity (km/s)

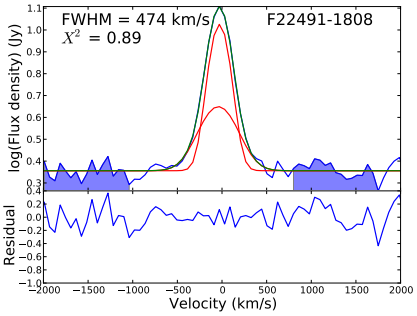
FWHM = 474 km/s
X^2 = 0.89
F22491-1808
log(Flux density) (Jy)
Residual
Velocity (km/s)

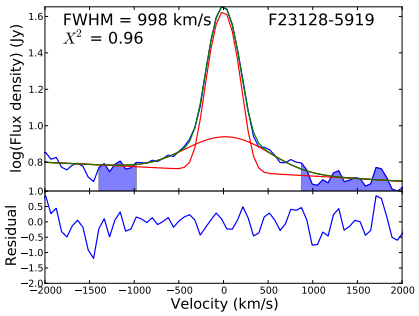
FWHM = 998 km/s
X^2 = 0.96
F23128-5919
log(Flux density) (Jy)
Residual
Velocity (km/s)

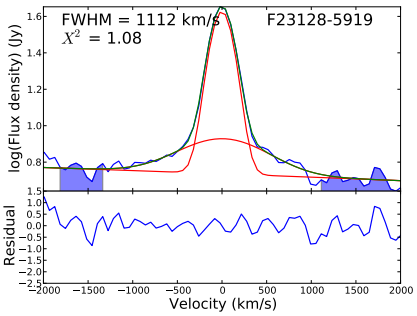
FWHM = 1112 km/s
X^2 = 1.08
F23128-5919
log(Flux density) (Jy)
Residual
Velocity (km/s)

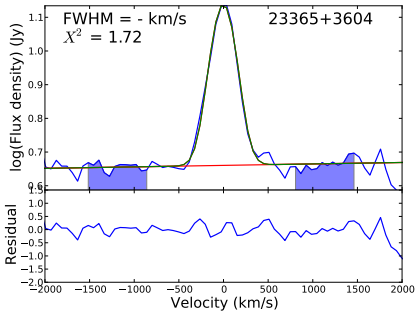
FWHM = - km/s
X^2 = 1.72
23365+3604
log(Flux density) (Jy)
Residual
Velocity (km/s)

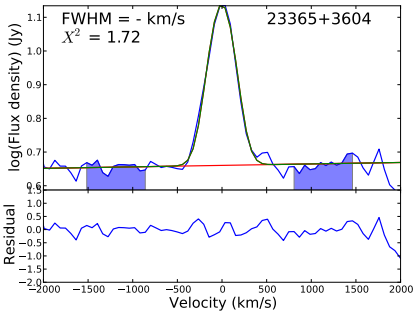
FWHM = - km/s
X^2 = 1.72
23365+3604
log(Flux density) (Jy)
Residual
Velocity (km/s)

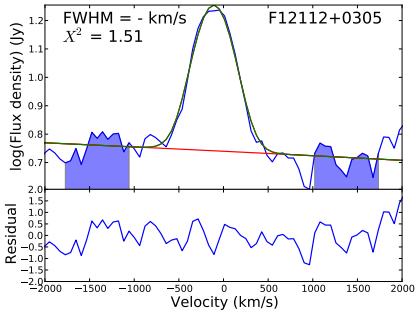
FWHM = - km/s
X^2 = 1.51
F12112+0305
log(Flux density) (Jy)
Residual
Velocity (km/s)

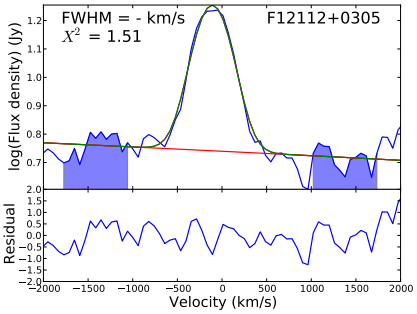
FWHM = - km/s
X^2 = 1.51
F12112+0305
log(Flux density) (Jy)
Residual
Velocity (km/s)

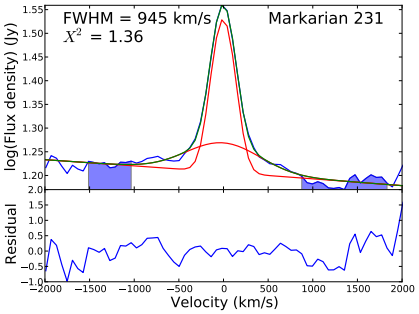
FWHM = 945 km/s
X^2 = 1.36
Markarian 231
log(Flux density) (Jy)
Residual
Velocity (km/s)

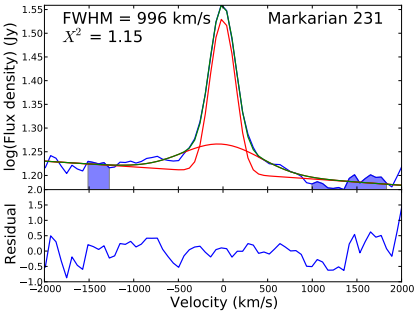
FWHM = 996 km/s
X^2 = 1.15
Markarian 231
log(Flux density) (Jy)
Residual
Velocity (km/s)

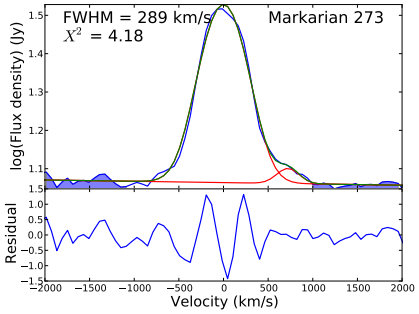
FWHM = 289 km/s
X^2 = 4.18
Markarian 273
log(Flux density) (Jy)
Residual
Velocity (km/s)

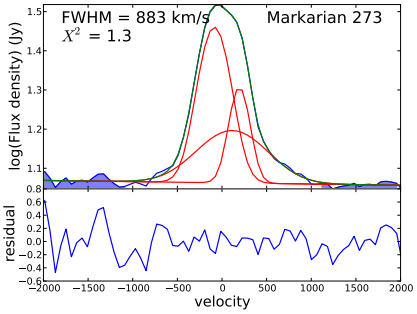
FWHM = 883 km/s
X^2 = 1.3
Markarian 273
log(Flux density) (Jy)
residual
velocity

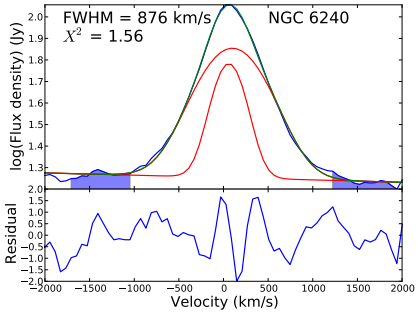
FWHM = 876 km/s
X^2 = 1.56
NGC 6240
log(Flux density) (Jy)
Residual
Velocity (km/s)

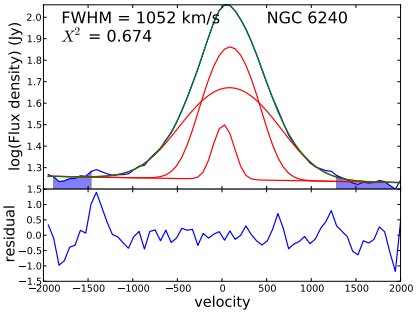
FWHM = 1052 km/s
X^2 = 0.674
NGC 6240
log(Flux density) (Jy)
residual
velocity

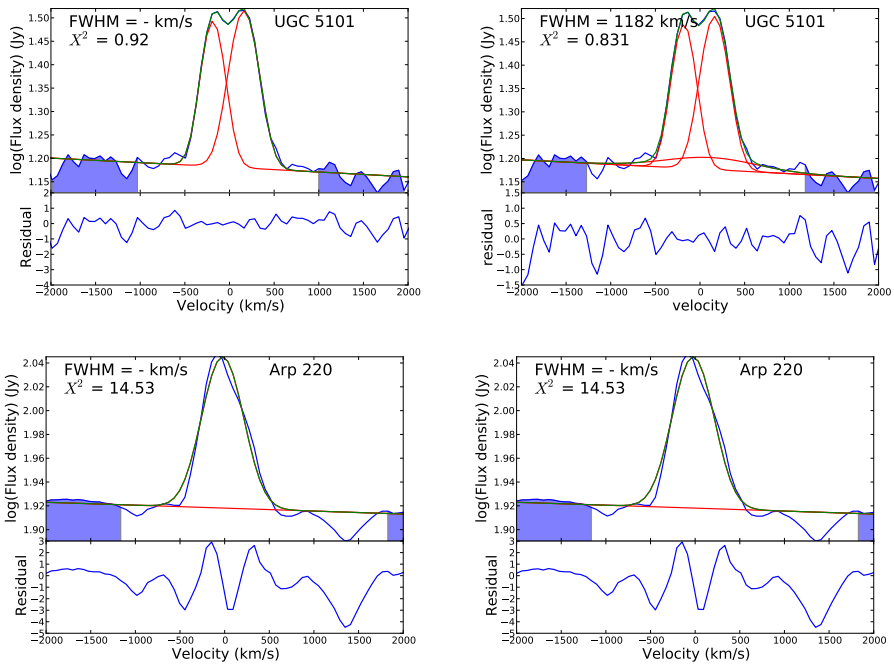

Fig. 6.— Gaussian fits to [CII] spectra: the flux density in the upper panel is shown in logarithmic scale, to make the faint wings stand out. The residual in the lower panel is given in linear scale. The FWHM of the broad component and the reduced χ^2 value is given in the figure. The PACS spectral resolution is 240 km s^{-1} FWHM. Each source has been fitted twice with different placements of the continuum, as shown by the shaded area.

Table 5. Gaussian fits

Name	h_1	m_1	$FWHM_1$	h_2	m_2	$FWHM_2$	h_3	m_3	$FHWM_3$	χ^2
F05189-2524	7.43	6	363	0.86	-609	327	...	...	...	1.43
F05189-2524	6.82	7	319	0.84	-131	1237	...	...	...	1.45
07251-0248	4.95	66	449	...	...	...	...	...	...	1.18
07251-0248	4.76	69	426	0.29	-78	1507	...	...	...	1.29
F08572+3915	5.6	-31	351	0.29	-52	1372	...	...	...	0.81
F08572+3915	5.62	-31	352	0.34	-9	1799	...	...	...	1.0
09022-3615	20.58	51	410	10.35	-106	734	...	...	...	0.76
09022-3615	20.58	51	410	10.35	-106	734	...	...	...	0.76
F10565+2448	29.89	0	301	3.37	20	911	...	...	...	0.87
F10565+2448	29.91	0	301	3.36	16	918	...	...	...	0.88
13120-5453	51.24	84	414	...	...	...	...	...	...	3.49
13120-5453	50.72	84	408	1.01	45	1803	...	...	...	2.41
F14348-1447	12.15	-122	383	2.27	-174	924	...	...	...	1.51
F14348-1447	12.13	-122	383	2.28	-174	914	...	...	...	1.35
F14378-3651	5.87	156	308	...	...	...	...	...	...	2.59
F14378-3651	5.53	157	286	0.4	132	667	...	...	...	3.9
F15250+3608	5.9	51	362	...	...	...	...	...	...	2.32
F15250+3608	5.9	51	362	...	...	...	...	...	...	2.32
F17207-0014	26.32	-1	533	...	...	...	...	...	...	2.71
F17207-0014	26.32	-1	533	...	...	...	...	...	...	2.71
F19297-0406	6.76	-28	413	3.33	-40	690	...	...	...	1.04
F19297-0406	9.46	-35	472	0.67	178	1415	...	...	...	0.9
19542+1110	3.5	81	366	...	...	...	...	...	...	1.77
19542+1110	3.5	81	366	...	...	...	...	...	...	1.77
F20551-4250	21.44	-14	302	2.98	41	737	...	...	...	2.75
F20551-4250	22.0	-13	307	2.52	59	873	...	...	...	4.12
F22491-1808	10.33	-30	300	...	...	...	...	...	...	1.22
F22491-1808	8.34	-28	259	2.19	-40	474	...	...	...	0.89
F23128-5919	36.73	-1	307	3.08	38	998	...	...	...	0.96
F23128-5919	36.92	-1	308	3.04	14	1112	...	...	...	1.08
F23365+3604	9.18	-2	320	...	...	...	...	...	...	1.72
F23365+3604	9.18	-2	320	...	...	...	...	...	...	1.72

Table 5—Continued

Name	h_1	m_1	$FWHM_1$	h_2	m_2	$FWHM_2$	h_3	m_3	$FHWM_3$	χ^2
F12112+0305	12.46	-108	483	...	...	...	...	...	...	1.51
F12112+0305	12.46	-108	483	...	...	...	...	...	...	1.51
Mrk 231	17.79	-3	291	2.47	-8	945	...	...	...	1.36
Mrk 231	17.9	-3	292	2.4	-20	996	...	...	...	1.15
Mrk 273	22.19	0	561	1.09	722	289	...	...	...	4.18
Mrk 273	17.33	-85	394	8.74	194	258	4.17	114	885	1.3
NGC 6240	42.82	59	415	53.63	100	876	...	...	...	1.56
NGC 6240	14.04	17	248	55.25	90	570	29.45	86	1053	0.67
UGC 5101	15.91	-186	298	17.65	160	357	...	...	...	0.92
UGC 5101	15.69	-181	295	16.96	161	340	0.91	118	1182	0.83
Arp 220	28.15	-22	521	...	...	...	...	...	...	14.53
Arp 220	28.15	-22	521	...	...	...	...	...	...	14.53

Note. — Parameters of Gaussian fits to the [CII] spectra. The units are Jansky for the height and $\mathrm{km\,s^{-1}}$ for the mean and FWHM. $\chi^2 = \frac{1}{N-n-1}\Sigma_{i=1}^{N}(obs_i - fit_i)^2/\sigma^2$, with N the number of data points in the spectrum, n the number of free parameters during the fit, and σ the RMS in the continuum. Each source has been fitted twice with different placements of the continuum, and appears therefore twice in the table.